

Diverse Properties of Interstellar Medium Embedding Gamma-Ray Bursts at the Epoch of Reionization

Renyue Cen¹ and Taysun Kimm²

ABSTRACT

Analysis is performed on ultra-high resolution large-scale cosmological radiation-hydrodynamic simulations to, for the first time, quantify the physical environment of long-duration gamma-ray bursts (GRBs) at the epoch of reionization. We find that, on parsec scales, 13% of GRBs remain in high density ($\geq 10^4 \text{cm}^{-3}$) low-temperature star-forming regions, whereas 87% of GRBs occur in low-density ($\sim 10^{-2.5} \text{cm}^{-3}$) high temperature regions heated by supernovae. More importantly, the spectral properties of GRB afterglows, such as the neutral hydrogen column density, total hydrogen column density, dust column density, gas temperature and metallicity of intervening absorbers, vary strongly from sightline to sightline. Although our model explains extant limited observationally inferred values with respect to circumburst density, metallicity, column density and dust properties, a substantially larger sample of high- z GRB afterglows would be required to facilitate a statistically solid test of the model. Our findings indicate that any attempt to infer the physical properties (such as metallicity) of the interstellar medium of the host galaxy based on a very small number of (usually one) sightlines would be precarious. Utilizing high- z GRBs to probe interstellar medium and intergalactic medium should be undertaken properly taking into consideration the physical diversities of the interstellar medium.

Subject headings: Methods: numerical, hydrodynamics, Galaxies: formation, reionization, Gamma-Ray bursts

1. Introduction

Very high redshift ($z \geq 6$) gamma-ray bursts (GRBs) (e.g., Greiner et al. 2009; Tanvir et al. 2009; Cucchiara et al. 2011) provide an excellent probe of both the interstellar (ISM) and intergalactic medium (IGM) at the epoch of reionization (EoR) using absorption spectrum techniques thanks to their simple power-law afterglow spectra and high luminosity (Lamb & Reichart 2000), complimentary to quasar absorption spectrum observations (Fan et al. 2006). Here we present a first, detailed analysis of the physical properties of ISM surrounding GRBs, utilizing state-of-the-art radiation-hydrodynamic simulations, with the hope that they may aid in proper interpretations of observations of GRB afterglows at EoR with respect to both ISM and IGM.

¹Princeton University Observatory, Princeton, NJ 08544; cen@astro.princeton.edu

²Princeton University Observatory, Princeton, NJ 08544; kimm@astro.princeton.edu

2. Simulations

The simulations are performed using the Eulerian adaptive mesh refinement code, RAMSES (Teyssier 2002, ver. 3.07), with concurrent multi-group radiative transfer (RT) calculation (Rosdahl et al. 2013). The reader is referred to Kimm & Cen (2014) for details. Notably, a new treatment of supernova feedback is implemented, which is shown to capture the Sedov solution for all phases (from early free expansion to late snowplow). The initial condition for the cosmological simulations is generated using the MUSIC software (Hahn & Abel 2011), with the WMAP7 parameters (Komatsu et al. 2011): $(\Omega_m, \Omega_\Lambda, \Omega_b, h, \sigma_8, n_s = 0.272, 0.728, 0.045, 0.702, 0.82, 0.96)$. The total simulated volume of $(25\text{Mpc}/h)^3$ (comoving) is covered with 256^3 root grids, and 3 more levels are added to a rectangular region of $3.8 \times 4.8 \times 9.6$ Mpc to achieve a high dark matter mass resolution of $m_{\text{dm}} = 1.6 \times 10^5 M_\odot$. In the zoomed-in region, cells are further refined (12 more levels) based on the density and mass enclosed within a cell. The corresponding maximum spatial resolution of the simulation is 4.2 pc (physical). The simulation is found to be consistent with a variety of observations, including the luminosity function at $z \sim 7$.

Normal and runaway star particles are created in convergent flows with a local hydrogen number density $n_{\text{th}} \geq 100 \text{ cm}^{-3}$ (FRU run, Kimm & Cen 2014), based on the Schmidt law (Schmidt 1959). Note that the threshold is motivated by the density of a Larson-Penston profile (Larson 1969; Penston 1969) at $0.5\Delta x_{\text{min}}$, $\rho_{\text{LP}} \approx 8.86c_s^2/\pi G \Delta x_{\text{min}}^2$, where c_s is the sound speed at the typical temperature of the ISM ($\sim 30\text{K}$) and Δx_{min} is the finest cell resolution. Additionally, we ensure that the gas is Jeans unstable, and that the cooling time is shorter than the dynamical time (e.g. Cen & Ostriker 1992). We assume that 2% of the star-forming gas is converted into stars per its free-fall time (t_{ff}) (Krumholz & Tan 2007). The mass of each star particle is determined as $m_\star = \alpha N_p \rho_{\text{th}} \Delta x_{\text{min}}^3$, where ρ_{th} is the threshold density, and α is a parameter that controls the minimum mass of a star particle ($m_{\star, \text{min}}$). N_p is an integer multiple of $m_{\star, \text{min}}$ to be formed in a cell, which is drawn from a Poisson random distribution, $P(N_p) = (\lambda^{N_p}/N_p!) \exp(-\lambda)$ with the Poissonian mean $\lambda \equiv \epsilon_\star \left(\frac{\rho \Delta x^3}{m_{\star, \text{min}}} \right) \left(\frac{\Delta t_{\text{sim}}}{t_{\text{ff}}} \right)$, where Δt_{sim} is the simulation time step. The resulting minimum mass of a normal (runaway) star particle is $34.2 M_\odot$ ($14.6 M_\odot$). We adopt the Chabrier initial mass function to compute the mean frequency of Type II supernova explosions per solar mass ($0.02 M_\odot^{-1}$). Dark matter halos are identified using the Amiga halo finder (Knollmann & Knebe 2009). This yields 731 halos of mass $10^8 \leq M_{\text{vir}} < 3 \times 10^{10} M_\odot$ at $z = 7$. We adopt the assumption that long-duration GRB rate is proportional to type II supernova rate; short-duration GRBs are not addressed here since they appear not to be associated with massive stars and are hosted by elliptical galaxies (Berger 2013). For our analysis we use all snapshots between $z = 7.5$ and $z = 7$.

3. Results

We present results from our simulations and make comparisons to available observations. As will be clear later, we generally find broad agreement between our model and observations, although larger observational samples of GRB afterglows would be needed to fully test the model.

3.1. Properties of Embedding Interstellar Medium on Parsec Scales

We first describe the physical conditions of the ISM that embeds GRBs on pc scales. The left (right) panel of Figure 1 shows the distribution of GRB rate in the density-temperature (density-metallicity) parameter space. We see two separate concentrations of GRBs in the $n - T$ plane, with (n_H, T) equal to $(10^{-2.5}\text{cm}^{-3}, 10^{7.5}\text{K})$ and $(10^{4.0}\text{cm}^{-3}, 10^{3.8}\text{K})$, respectively. It must be made clear that the density and temperature are defined on the local gas cell of scale of a few pc that a GRB sits. The appearance of GRB afterglow spectra depends, in most case, more strongly on the properties of gas along the line of sight rather than the gas immediately embedding them, as will be shown later. It is seen that most of the GRBs reside in the low density, high temperature peak, contributing to 87% of GRBs. It is easy to identify two corresponding concentrations in the $Z - n$ plane in the right panel: the low density, high temperature peak corresponds the high metallicity peak in the range $[-1.5, 0.5]$ in solar units, while the high density, low temperature peak corresponds the low metallicity peak in the range $[-2, -1]$. We note that super solar metallicities in hot winds driven by type II supernova explosions in starburst galaxies in conditions similar to those of our simulated galaxies are locally observed. For example, Konami et al. (2011) observe metallicity of hot X-ray gas of 2 – 3 times the solar value in M82. Martin et al. (2002) find that the best fit model for the hot X-ray gas metallicity in dwarf starburst galaxy NGC 1569 is solar, although a metallicity as high as 5 times solar still gives χ^2 value only about 0.1% larger than the best fit model; on the contrary, the model with 0.25 times solar has much worse χ^2 value. The extant observations of GRB afterglow spectra do not have the capability to detect the metallicity of the X-ray absorbing medium of relatively low column density. Metallicities of lower temperature gas phases are observed and are predicted to be substantially sub solar, as will be shown in Figure 3 later.

The $(n_H, T) = (10^{4.0}\text{cm}^{-3}, 10^{3.8}\text{K})$ peak coincides with the cores of dense gas clouds in the simulation, where star formation is centered. The temperature of $10^{3.8}\text{K}$ is mostly produced by atomic hydrogen cooling and the lower temperature extension due to metal cooling included in the simulation. As a numerical example, for a gas parcel of density 10^4cm^{-3} , temperature of 10^4K and metallicity of 1% of solar value, the cooling time is about 400 yrs, which is much shorter than relevant dynamic time scales. It is thus clear that the cold density phase seen our simulation is easily understandable. However, due to lack of treatment for molecular hydrogen cooling, gas is unable to cool significantly below $\sim 10^4\text{K}$. Had we included molecular hydrogen cooling and low temperature metal cooling, we expect the gas to cool approximately isobarically to about 20K. Thus, we prefer not to infer any observable properties of GRBs that would depend strongly on the nature of this cold gas phase, such as molecular clouds. It is more appropriate to treat $(n_H, T) = (10^{4.0}\text{cm}^{-3}, 10^{3.8}\text{K})$ as bounds: $(n_H, T) = (> 10^{4.0}\text{cm}^{-3}, < 10^{3.8}\text{K})$. This is also why we present our results for the high-density low-temperature regions as bounds in the abstract and conclusions sections as well as places where clarification is helpful. The noticeable sub-dominance of GRBs residing in very high density ($n \sim 10^4\text{cm}^{-3}$), star-forming regions suggests that a large number of stars are displaced from their birth clouds. This may be achieved by a substantial relative motions between stars and their birth clouds due to hydrodynamic interactions of the later or dynamical effects of stars. As a numerical illustration for the former possibility, a relative motion of 10 km/s between the birth cloud and the

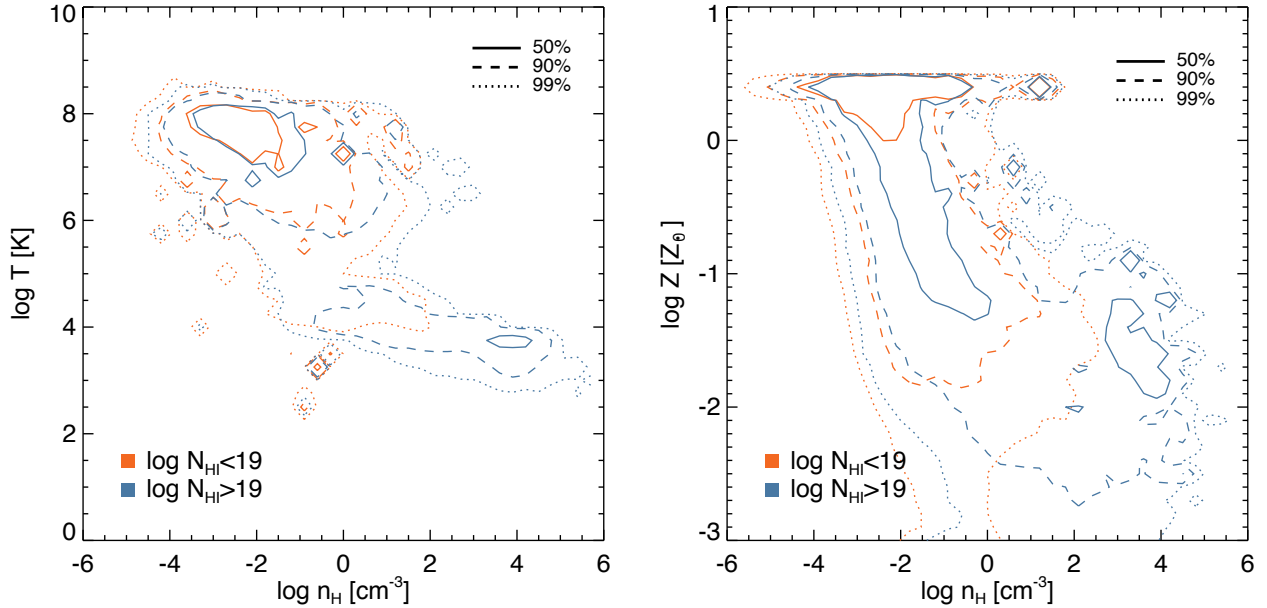


Fig. 1.— **Left panel:** shows the distribution of GRB rate in the density-temperature ($n - T$) parameter space. Note that the density and temperature are defined on the local gas cell of scale of a few pc that a GRB sits in and it will be made clear later that the appearance of GRB afterglows is in most cases more dependent on the properties of gas along the line of sight. We have further divided the GRBs into two groups with respect to intervening neutral hydrogen column density: $N_{\text{HI}} > 10^{19}\text{cm}^{-2}$ (red) and $N_{\text{HI}} < 10^{19}\text{cm}^{-2}$ (blue), details of which will be given in subsequent figures. The contour levels specified indicate the fraction of GRBs enclosed. **Right panel:** shows the distribution of GRB rate in the density-metallicity ($n - Z$) parameter space.

star would yield a displacement of 100pc in a lifetime of 10Myr. We note that the runaway OB stars in our simulation have typical velocities relative to the birth clouds of 20 – 40 km/s. Thus the runaway OB stars have contributed significantly to the displacing GRBs from their birth clouds. The GRBs being in hot low density environment is also a result of supernova heating by earlier supernovae exploding in the birth clouds. We estimate that these two effects are responsible about equally for placing most of the GRBs in low-density high temperature regions. While it is not possible to locate GRBs within the host galaxies at high redshift at this time, observations of low redshift GRBs may still be instructive. Le Floc’h et al. (2012) show that GRB 980425 occurring in a nearby ($z = 0.0085$) SBC-type dwarf galaxy appears to be displaced from the nearest H II region by 0.9kpc, which is in fact significantly larger than the displacement distances for the vast majority of our simulated GRBs in high redshift galaxies.

Interestingly, the optical afterglow luminosity has a bimodal distribution at 12 hours after trigger (Nardini et al. 2008). The bimodal distribution of volumetric density seen in the left panel of Figure 1 alone should produce a bimodal distribution of the afterglows with respect to break frequencies, luminosities, and break times, etc (e.g., Sari et al. 1998). We cannot make detailed comparisons, because the circumburst density of the high n_H GRB subset is underestimated due to our limited resolution and because it remains uncertain if the appearance of GRB afterglows

would also depend strongly on intervening material (dust obscuration, etc). It is suggestive that the complex situations seen in simulations may account for the observed bimodality of afterglows without having to invoke intrinsic bimodality of GRBs.

3.2. Strong Variations of Intervening Gas and Dust along Different Sightlines

One of the most important points that this paper hopes to highlight and convey is that the appearances of the afterglows of GRBs are not solely determined by the circumburst medium in their immediate vicinity (e.g., the physical conditions shown in Figure 1 are on pc scales centered on GRBs). They also strongly depend on the line of sight beyond the immediate circumburst medium through the ISM in the host galaxy, which we now quantify. Let us first give the meaning for our chosen value of the intervening neutral hydrogen column density $N_{HI} = 10^{19}\text{cm}^{-2}$, which is used in Figure 1 to separate GRBs into separate groups. Figure 2 shows the distribution of neutral hydrogen column density integrated along the line of sight for all GRBs, separately for halos in five mass ranges. A bimodal distribution of N_{HI} is seen, peaked at $N_{HI} \sim 10^{21-22}\text{cm}^{-2}$ and $N_{HI} \sim 10^{16-17}\text{cm}^{-2}$, respectively, well separated by $N_{HI} \sim 10^{19}\text{cm}^{-2}$. It is clear that the bimodality exists for all halo masses surveyed. The low N_{HI} peak is rather broad, extending all the way to $N_{HI} = 10^{11}\text{cm}^{-2}$, suggesting some locations of GRBs well into the diffused hot ISM. There is a noticeable dip in the neutral hydrogen column density distribution at $\sim 10^{14}\text{cm}^{-2}$ for the most massive galaxies of $\geq 10^{10} M_{\odot}$. We attribute this to more significant shock heating in the most massive halos.

Returning to Figure 1, it is now easy to see that the GRBs in the low N_{HI} ($\leq 10^{19}\text{cm}^{-2}$) peak in Figure 2 is composed of only one set of GRBs situated in low density environment around ($10^{-2.5}\text{cm}^{-3}, 10^{7.5}\text{K}$), seen as the red contours in Figure 1. The high N_{HI} ($\geq 10^{19}\text{cm}^{-2}$) peak in Figure 2, on the other hand, consists of a combination of two separate populations with distinctly different circumburst medium, which correspond to two separate loci of the blue contours at ($10^{-2.5}\text{cm}^{-3}, 10^{7.5}\text{K}$) and ($10^{4.0}\text{cm}^{-3}, 10^{3.8}\text{K}$) in Figure 1.

The apparently two different groups of GRBs situated around $(n_H, T) = (10^{-2.5}\text{cm}^{-3}, 10^{7.5}\text{K})$ - one with low $N_{HI} \leq 10^{19}\text{cm}^{-2}$ (red) and the other with low $N_{HI} \geq 10^{19}\text{cm}^{-2}$ (blue) - are due entirely to the line of sight through the ISM of the host galaxy. Overall, we find that 38% of GRBs have $N_{HI} \leq 10^{17}\text{cm}^{-2}$ (i.e., optically thin to Lyman continuum), whereas 44% have $N_{HI} \geq 10^{20.3}\text{cm}^{-2}$ (i.e., containing a damped Lyman-alpha system). It is clear that various properties of the afterglows of GRBs, even sitting in the same very local environment on pc scales, may appear different due to different intervening interstellar gas and dust along the line of sight through the host galaxy. In summary so far, there are three separate populations of GRB afterglows are expected, if our model is correct. One might classify them in the following simple way: (1) HnHN=(high volumetric density $n \sim 10^4\text{cm}^{-3}$, high neutral column density $N_{HI} \geq 10^{19}\text{cm}^{-2}$), (2) LnHN=(low volumetric density $n \sim 10^{-2.5}\text{cm}^{-3}$, high neutral column density $N_{HI} \geq 10^{19}\text{cm}^{-2}$), (3) LnLN=(low volumetric density $n \sim 10^{-2.5}\text{cm}^{-3}$, high neutral column density $N_{HI} \leq 10^{19}\text{cm}^{-2}$). Again, types (2) and (3) are a result of different viewing angles, where type (2) is due to viewing angles through largely hot ionized gas and type (3) viewing angles going through cold and dense gas in addition.

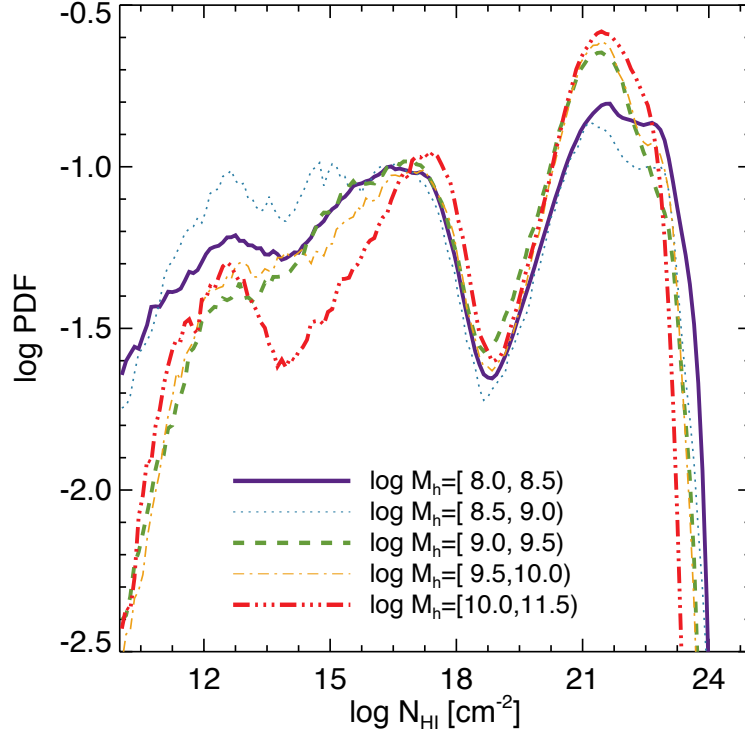


Fig. 2.— shows the probability distribution functions (PDF) of neutral hydrogen column density for all GRBs, separated according to the halo masses indicated in the legend.

Laskar et al. (2014) analyze multi-wavelength observations of the afterglow of GRB 120521C ($z \sim 6$) and re-analyze two previous GRBs at $z > 6$ (GRB 050904 and 090423), and conclude that the circumburst medium has a volumetric density of $n_H \leq 0.05 \text{cm}^{-3}$ that is constant. The GRBs in the LnHN or LnLN group provide the right match to the observations. While the statistic is still small, it is expected that about 87% of GRBs should arise in either the LnHN or LnLN group.

Observations of GRB 050904 at $z = 6.3$ reveal that it contains a damped Lyman alpha systems (DLAs) system in the host galaxy of column density $N_{HI} = 10^{21.6} \text{cm}^{-2}$ and metallicity of $Z = -2.6$ to -1 (Totani et al. 2006; Kawai et al. 2006). Based on X-ray observations, Campana et al. (2007) conclude that $Z \geq 0.03 Z_\odot$ for GRB 050904. The evidence thus suggests that GRB 050904 likely resides in a dense environment, although it cannot be completely sure because the metallicity range of the low-density peak (right panel of Figure 1) overlaps with the observed range. It is useful at this juncture to distinguish between the metallicity of the local environment of a GRB and that of absorbers in the GRB afterglow spectrum.

Let us now turn to the expected metallicity of UV/optical absorbers in the GRB afterflow spectra. Figure 3 shows the PDFs of total hydrogen-column-density-weighted metallicity of gas along the line of sight, excluding gas hotter than 10^6K , for the three sub-populations of GRBs. We see that for all three GRB groups the metallicity of the absorbers in the GRB spectra peaks in the range -3 to -1 . Thus, it is now clear that our model can easily account for the observed properties of GRB 050904. The additional evidence that, based on the analysis of the equivalent width ratio of the fine structure transition lines Si II* $\lambda 1264.7 \text{\AA}$ and Si II $\lambda 1260.4 \text{\AA}$, infers the electron density

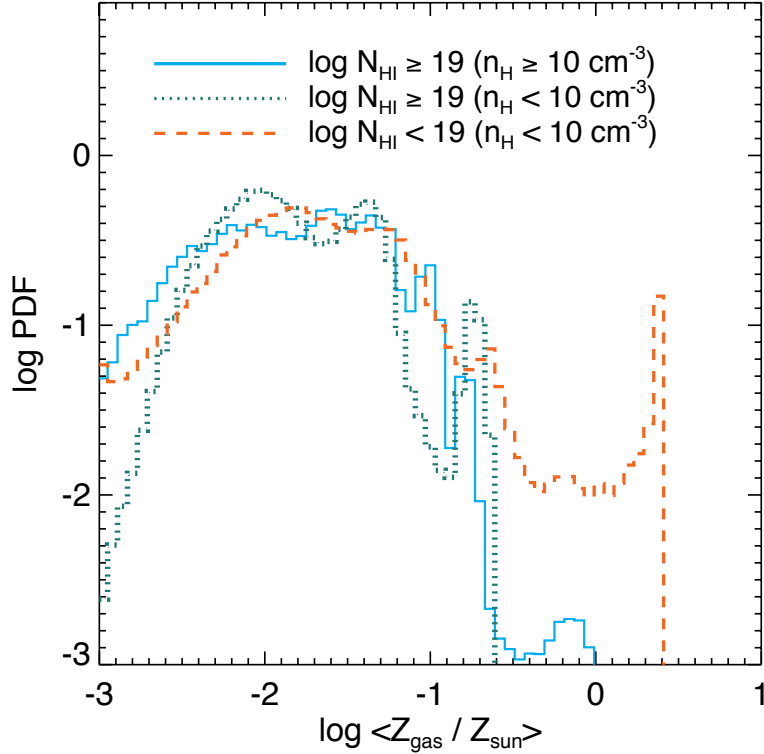


Fig. 3.— shows the PDFs of total hydrogen column density weighted metallicity of gas along the line of sight, excluding gas hotter than 10^6K , for the three sub-populations of GRBs: GRBs in $(n_H, T) = (10^{-2.5}\text{cm}^{-3}, 10^{7.5}\text{K})$ with $N_{\text{HI}} \leq 10^{19}\text{cm}^{-2}$ (red dashed, LnLN group), $(n_H, T) = (10^{-2.5}\text{cm}^{-3}, 10^{7.5}\text{K})$ with $N_{\text{HI}} \geq 10^{19}\text{cm}^{-2}$ (green dotted, LnHN group), and $(n_H, T) = (10^{4.0}\text{cm}^{-3}, 10^{3.75}\text{K})$ with $N_{\text{HI}} \geq 10^{19}\text{cm}^{-2}$ (blue solid, HnHN group).

of $\log n_e = 2.3 \pm 0.7$. Furthermore, the magnitude of the optical afterglow at 3.4 days after the burst favors a high density circumburst medium. In combination, it appears that GRB 050904 is likely in a dense environment being to the HnHN group. This appears to be at some minor odds with our model, since we only expect that 13% of GRBs to arise in the HnHN group. It would be highly desirable to obtain a larger sample of high- z GRBs to provide a statistically firmer test.

Analyses of observations of GRB 130606A at $z = 5.9$ indicate that it likely contains a sub-DLA system of $N_{\text{HI}} \sim 10^{19.8}\text{cm}^{-2}$ in the host galaxy (Totani et al. 2013; Castro-Tirado et al. 2013). The inferred low metallicity of -1.8 to -0.8 in solar units (Castro-Tirado et al. 2013) and -1.3 to -0.5 (Chornock et al. 2013), in conjunction with the N_{HI} , suggests that GRB 130606A may reside in a low density environment with a foreground sub-DLA system in the host galaxy. This proposal is consistent with the evidence of detection of highly ionized species (e.g., N V and Si IV) (Castro-Tirado et al. 2013). It seems likely that GRB 130606A belongs to the LnHN group.

It is easy to see that in our model the metallicity distribution of UV/optical absorbers in GRB afterglow spectra is wide, which itself is due to the very inhomogeneous metallicity distributions in the ISM of the host galaxies. Thus, it would be a rather chancy practice trying to infer the metallicity of the host galaxy solely based on a small number of (typically one) GRB afterglow absorption spectra.

The reader has already seen clearly that the distributions of all concerned physical quantities, including metallicity, density, total and neutral hydrogen column density, are wide. We will add yet one more quantity and show the cumulative distributions of the ratio of neutral hydrogen to total hydrogen column density for the three groups in the right panel of Figure 4. We see that for GRBs in the LnLN group the neutral hydrogen to total hydrogen column ratio is significantly less than unity. Even for the HnHN and LnHN groups, (10%,14%) of GRBs have the ratio less than 0.1. In other words, it is generally a pretty bad assumption that the apparent absorbers in the GRB afterglow spectra are mainly neutral. This indicates that the so-called “missing gas problem” (e.g., Schady et al. 2011) may be accommodated in this model.

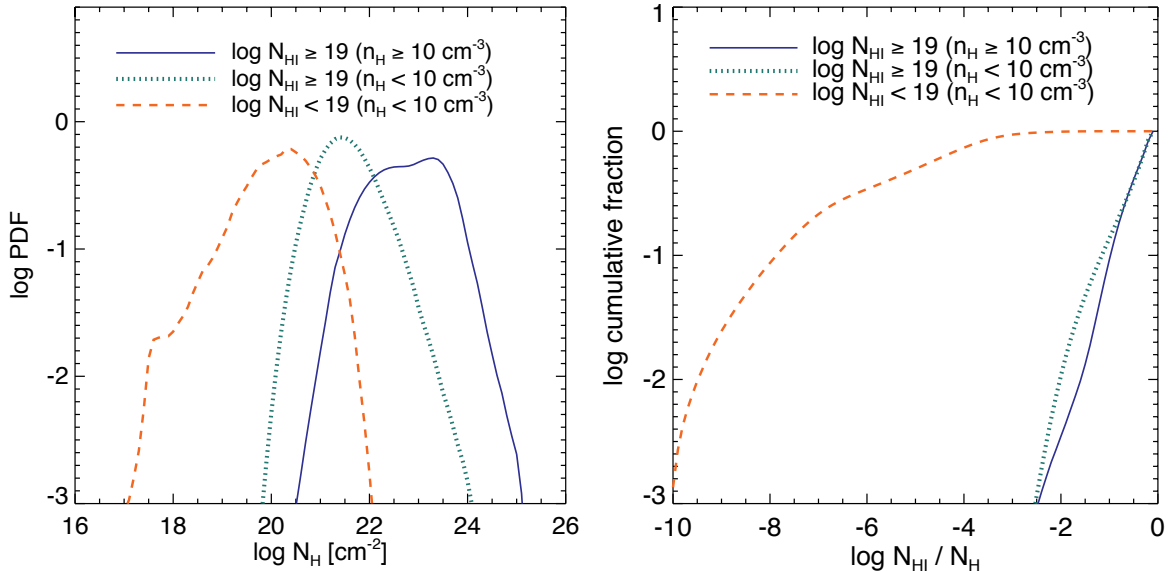


Fig. 4.— **Left panel:** shows the PDFs of total hydrogen column density for the three sub-populations of GRBs: GRBs in $(n_H, T) = (10^{-2.5}\text{cm}^{-3}, 10^{7.5}\text{K})$ with $N_{\text{HI}} \leq 10^{19}\text{cm}^{-2}$ (red dashed, LnLN group), $(n_H, T) = (10^{-2.5}\text{cm}^{-3}, 10^{7.5}\text{K})$ with $N_{\text{HI}} \geq 10^{19}\text{cm}^{-2}$ (green dotted, HnLN group), and $(n_H, T) = (10^{4.0}\text{cm}^{-3}, 10^{3.75}\text{K})$ with $N_{\text{HI}} \geq 10^{19}\text{cm}^{-2}$ (blue solid, HnHN group). **Right panel:** shows the cumulative PDFs of the ratio of N_{HI}/N_H .

The left panel of Figure 4 shows the PDFs of the total hydrogen column density for the three sub-populations of GRBs, which is most relevant for probing GRB X-ray afterglows and hence a useful test of our model. One expectation from our model is that the vast majority of GRBs sitting in low density circumburst medium (LnHN + LnLN) do not have Compton thick obscuring gas. This prediction is verifiable with a combination of afterglow light curves and X-ray observations. On the other hand, one expects from our model that a significant fraction of the GRBs sitting in high density circumburst medium (HnHN) have an extended high N_H tail and dominate the GRBs with $N_H \geq 10^{23}\text{cm}^{-2}$. Quantitatively, we find that (45%, 3%) of GRBs have $N_H \geq (10^{23}, 10^{24})\text{cm}^{-2}$; it is noted that these two numbers are likely lower bounds due to possible numerical resolution effects. As already noted earlier, it is seen from the right panel that the GRBs in the LnLN group are intervened by highly ionized gas peaking at an average neutral fraction of $\sim 10^{-4}$, with no cases having a neutral fraction exceeding 10^{-1} . In contrast, for GRBs in both the HnLN and HnHN

groups, more than 50% of them have an average neutral fraction greater than $\sim 10^{-1}$.

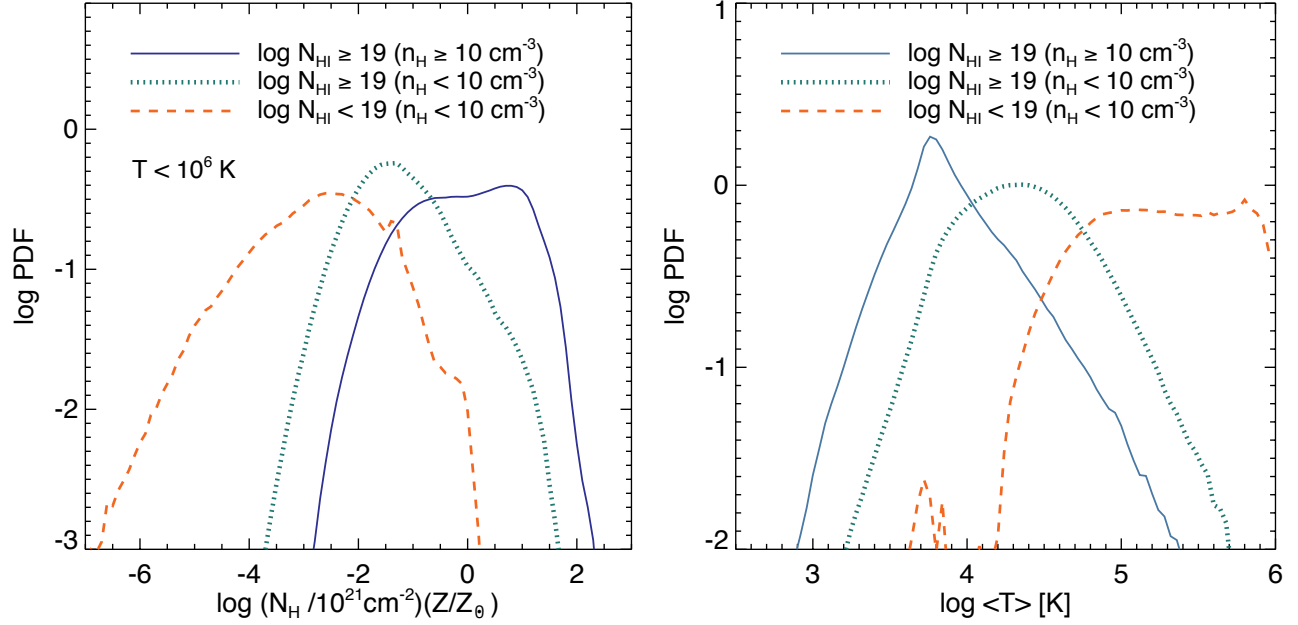


Fig. 5.— **Left panel:** shows the PDFs of metallicity weighted total hydrogen column density, $(N_H/10^{21}\text{cm}^{-2})(Z/Z_\odot)$, excluding gas with temperature greater than 10^6K , for the three sub-populations of GRBs: GRBs in $(n_H, T) = (10^{-2.5}\text{cm}^{-3}, 10^{7.5}\text{K})$ with $N_{\text{HI}} \leq 10^{19}\text{cm}^{-2}$ (red dashed), $(n_H, T) = (10^{-2.5}\text{cm}^{-3}, 10^{7.5}\text{K})$ with $N_{\text{HI}} \geq 10^{19}\text{cm}^{-2}$ (green dotted), and $(n_H, T) = (10^{4.0}\text{cm}^{-3}, 10^{3.75}\text{K})$ with $N_{\text{HI}} \geq 10^{19}\text{cm}^{-2}$ (blue solid). The exclusion of $\geq 10^6\text{K}$ gas is intended for the situation that dust is efficiently destroyed in hot gas. According to Draine (2003), $A_V \approx (N_H/10^{21}\text{cm}^{-2})(Z/Z_\odot)$. **Right panel:** shows the PDFs of gas temperature weighted by $N_H Z$, excluding gas with temperature greater than 10^6K .

We now turn to the issue of dust obscuration. The left panel of Figure 5 shows the PDFs of visual extinction A_V . It is noted that the simulation does not follow dust formation explicitly. Thus, we have adopted the well known empirical relation between metal column density and visual extinction: $A_V = (N_H/10^{21}\text{cm}^{-2})(Z/Z_\odot)$ (Draine 2003). While the applicability of the relation derived from local observations is uncertain, detailed analysis of galaxy colors at EoR suggest that the simulated galaxies based on this relations give rise to self-consistent results when comparing to observations (Kimm & Cen 2013; Cen & Kimm 2014). Moreover, direct observations of dust suggest that this relation holds well in other galaxies locally, and galaxies and damped Lyman alpha systems at moderate to high redshift (e.g., Draine et al. 2007; De Cia et al. 2013; Draine et al. 2014; Fisher et al. 2014). Nevertheless, it is possible that the normalization factor in front of the relation is probably uncertain to order of unity. It is evident that a significant fraction of GRBs in the high HnHL group (blue solid curve) are heavily dust obscured, with (53%, 16%) of GRBs in the HnHL group have $A_V \geq (1, 10)$. At the other extreme, we see that the GRBs in the LnLN group (red dashed curve) have negligible dust columns with no case of $A_V \geq 0.3$; nevertheless, it is worth pointing out that, even for this set of GRBs 12% has an $A_V \geq 0.03$ due largely to dust in high temperature gas. The GRBs in the LnHN group (green dotted curve) sits in between the above

two groups, with a small but non-negligible fraction (7%) at $A_V > 1$. Observationally, the issue of dust in high- z GRB hosts is less than settled. Zafar et al. (2010), based on a re-analysis of the multi-epoch data of the afterglow of GRB 050904 at $z = 6.3$, conclude that there is no evidence of dust. Given that the neutral column density of the in situ DLA for GRB 050904 is $N_{HI} = 10^{21.6} \text{cm}^{-2}$ and low metallicity $Z = -2.6$ to -1 (Totani et al. 2006; Kawai et al. 2006), an $A_V \sim 0.01$ is possible, if one adopts the lower metallicity value that is statistically allowed in our model (see the right panel of Figure 1). Thus, both the low extinction and a standard ratio of dust to metals are still consistent with the observations. Our model indicates that 9% of GRBs have $A_V \geq 1$. Thus, with a $z \geq 6$ GRB sample of size 11, one expects to see one GRBs with $n_H \sim 10^4 \text{cm}^{-3}$ that is significantly obscured by dust with $A_V > 1$. This may be testable with SWIFT data relatively soon.

The right panel of Figure 5 shows the PDFs of average gas temperature weighted by $N_H Z$, excluding gas with temperature greater than 10^6K (the exclusion is a crude way to say that dust in gas hotter than 10^6K is destroyed). The purpose of this plot is to provide an indication the diversity of intervening gas with dust. One notes that the lines of sight of HnHL GRBs contain dust in cold medium ($T \leq 10^4 \text{K}$), whereas those of high LnHN GRBs are dominated by dust residing in gas $T \sim 10^{4-5} \text{K}$, and the LnLN GRBs are intervened by dust in hotter gas of $T \geq 10^5 \text{K}$. Under the assumption that the hotter gas is presumably produced by shocks, which are more destructive to larger dust grains, one might suggest that dust becomes increasingly grayer from HnHL to LnHN to LnLN. One expectation is that some lines of sight, especially those for the HnLN and HnHN groups the total dust arise from multiple, different temperature regions. This may provide a physical explanation for the observational indications of multiple dust components (e.g., Zafar et al. 2012).

As a side note on the SFR of GRB hosts. Basa et al. (2012) place the star formation rate (SFR) of GRB 080913 at $z = 6.7$ to be less than $0.9 M_\odot/\text{yr}$. Berger et al. (2007) obtain an upper bound on the star formation rate of GRB 050904 at $z = 6.3$ less than $5.7 M_\odot/\text{yr}$. From the simulations we find that (42%, 57%, 66%) of GRBs occur in galaxies with SFR less than (0.3, 1.0, 3.0) M_\odot/yr . Thus, while simulations and observations are in good agreement, larger data sets are needed to place the comparisons on a solid statistical ground.

Finally, we must stress that the analysis performed here has focused on the ISM embedding the GRBs at EoR. The exact details of the state of the IGM at EoR are uncertain both observationally and theoretically. The theoretical difficulty is in part computational, because we do not have the capability to simulate a large enough volume to capture of the reionization of the IGM self-consistently, while still having enough resolution for the ISM. The goal of this work is to present the signatures of the ISM theoretically, which is lacking. It may be argued that the properties of ISM in galaxies are somewhat detached from the properties of the IGM on large scales; in other words, the observed spectra of GRB afterglows at EoR may be considered to be imprinted by both ISM and IGM as a linear superposition. Consequently, a proper understanding of the ISM will not only aid in the interpretation of the ISM of galaxies at EoR but also is highly needed for proper interpretation of the properties (neutral fraction, topology, etc) of the IGM at EoR.

4. Conclusions

We perform an analysis to quantify the physical condition of the ISM embedding GRBs as well as intervening gas in the host galaxies at high redshift $z \geq 6$. Our analysis is based on a zoomed-in cosmological radiation hydrodynamics simulation of $3.8 \times 4.8 \times 9.6 \text{ Mpc}^3$ box (comoving) with 731 halos of mass $10^8 \leq M_{\text{vir}} < 3 \times 10^{10} M_{\odot}$ at $z = 7$ at high spatial ($\sim 4 \text{ pc}$, physical) and stellar mass resolution of $49 M_{\odot}$. The following are new findings.

On parsec scales, GRBs are concentrated in two regions in density-temperature-metallicity space, with (n_H, T, Z) being $(10^{-2.5} \text{ cm}^{-3}, 10^{7.5} \text{ K}, -1.5 \text{ to } 0.5)$ and $(> 10^{4.0} \text{ cm}^{-3}, < 10^{3.8} \text{ K}, -2.5 \text{ to } -1)$, consisting of 87% and 13% of GRBs, respectively. The appearance of GRB afterglows, however, also strongly depends on the line of sight thanks to varying physical properties of intervening gas and dust in the host galaxy, which in turn splits the low density peak into two subsets. As a result, three separate apparent groups of GRB afterglows composing of (13%, 37%, 50%) are expected to arise with the following physical properties: (1) a cold neutral circumburst gas of hydrogen density of $n_H \sim 10^4 \text{ cm}^{-3}$, neutral hydrogen column density 90% range of $N_{\text{HI}} \sim 10^{21.0} - 10^{23.3} \text{ cm}^{-2}$, total hydrogen column density 90% range of $N_{\text{H}} \sim 10^{21.6} - 10^{23.8} \text{ cm}^{-2}$, with (53%, 16%) having A_V greater than (1,10), (2) a hot circumburst gas of hydrogen density of $n_H \sim 10^{-2.5} \text{ cm}^{-3}$, neutral hydrogen column density 90% range of $N_{\text{HI}} \sim 10^{19.5} - 10^{22.3} \text{ cm}^{-2}$, total hydrogen column density 90% range of $N_{\text{H}} \sim 10^{20.6} - 10^{22.5} \text{ cm}^{-2}$, with (7%, 1%) having A_V greater than (1,10), (3) a hot circumburst gas of hydrogen density of $n_H \sim 10^{-2.5} \text{ cm}^{-3}$, neutral hydrogen column density 90% range of $N_{\text{HI}} \sim 10^{10.5} - 10^{18.0} \text{ cm}^{-2}$, total hydrogen column density 90% range of $N_{\text{H}} \sim 10^{18.7} - 10^{21.1} \text{ cm}^{-2}$, with (0.2%, 0%) having A_V greater than (1,10). Common among all three groups of GRBs is that the metallicity of proximity optical/UV absorbers in the afterglow spectra is expected to be in the range of $Z = -3$ to -1 .

The strikingly diverse physical properties - metallicity, neutral hydrogen column density, total column density, gas temperature, dust column - of intervening absorbers of GRB afterglows as well as the bimodal physical properties of local (parsec-scale) environment indicates that a solid statistical comparison between the model predictions and observations needs to await a large observational sample of GRBs at the EoR. It is obvious that the available small sample of GRB afterglows complicates the task of interpreting the ISM of a small number of GRB host galaxies and the additional task of inferring the state of the IGM at EoR. Nevertheless, utilizing high- z GRBs to probe interstellar medium and intergalactic medium must be undertaken properly taking into consideration the physical diversities of the interstellar medium. The analysis presented will provide a physical framework to be confronted by future observations statistically.

Fruchter et al. (2006) find that GRBs are more concentrated in the very brightest regions of their host galaxies than are the core-collapse supernovae. Our analysis so far has assumed that the two populations are just proportional to one another. One may turn the argument around and use the observed distributions of GRBs that depend on both embedding environment and intervening material to test the connection between GRBs and star formation. Needless to say, larger samples will be able to shed light on this extremely important issue, which will have strong bearings on relating GRB rates to cosmological reionization.

Acknowledgements

We would like to thank Omer Bromberg for discussion. Computing resources were in part provided by the NASA High- End Computing (HEC) Program through the NASA Advanced Supercomputing (NAS) Division at Ames Research Center. The research is supported in part by NSF grant AST-1108700 and NASA grant NNX12AF91G.

REFERENCES

- Basa, S., Cuby, J. G., Savaglio, S., Boissier, S., Clément, B., Flores, H., Le Borgne, D., & Mazure, A. 2012, *A&A*, 542, A103
- Berger, E. 2013, ArXiv e-prints
- Berger, E., Chary, R., Cowie, L. L., Price, P. A., Schmidt, B. P., Fox, D. B., Cenko, S. B., Djorgovski, S. G., Soderberg, A. M., Kulkarni, S. R., McCarthy, P. J., Gladders, M. D., Peterson, B. A., & Barger, A. J. 2007, *ApJ*, 665, 102
- Campana, S., Lazzati, D., Ripamonti, E., Perna, R., Covino, S., Tagliaferri, G., Moretti, A., Romano, P., Cusumano, G., & Chincarini, G. 2007, *ApJ*, 654, L17
- Castro-Tirado, A. J., Sánchez-Ramírez, R., Ellison, S. L., Jelínek, M., Martín-Carrillo, A., Bromm, V., Gorosabel, J., Bremer, M., Winters, J. M., Hanlon, L., Meegan, S., Topinka, M., Pandey, S. B., Guziy, S., Jeong, S., Sonbas, E., Pozanenko, A. S., Cunniffe, R., Fernández-Muñoz, R., Ferrero, P., Gehrels, N., Hudec, R., Kubánek, P., Lara-Gil, O., Muñoz-Martínez, V. F., Pérez-Ramírez, D., Štrobl, J., Álvarez-Iglesias, C., Inasaridze, R., Rumyantsev, V., Volnova, A., Hellmich, S., Mottola, S., Castro Cerón, J. M., Cepa, J., Göğüş, E., Güver, T., Önal Taş, Ö., Park, I. H., Sabau-Graziati, L., & Tejero, A. 2013, ArXiv e-prints
- Cen, R., & Kimm, T. 2014, *ApJ*, 782, 32
- Cen, R., & Ostriker, J. P. 1992, *ApJ*, 399, L113
- Chornock, R., Berger, E., Fox, D. B., Lunnan, R., Drout, M. R., Fong, W.-f., Laskar, T., & Roth, K. C. 2013, *ApJ*, 774, 26
- Cucchiara, A., Levan, A. J., Fox, D. B., Tanvir, N. R., Ukwatta, T. N., Berger, E., Krühler, T., Küpcü Yoldaş, A., Wu, X. F., Toma, K., Greiner, J., Olivares, F. E., Rowlinson, A., Amati, L., Sakamoto, T., Roth, K., Stephens, A., Fritz, A., Fynbo, J. P. U., Hjorth, J., Malesani, D., Jakobsson, P., Wiersema, K., O’Brien, P. T., Soderberg, A. M., Foley, R. J., Fruchter, A. S., Rhoads, J., Rutledge, R. E., Schmidt, B. P., Dopita, M. A., Podsiadlowski, P., Willingale, R., Wolf, C., Kulkarni, S. R., & D’Avanzo, P. 2011, *ApJ*, 736, 7
- De Cia, A., Ledoux, C., Savaglio, S., Schady, P., & Vreeswijk, P. M. 2013, *A&A*, 560, A88
- Draine, B. T. 2003, *ARA&A*, 41, 241

- Draine, B. T., Aniano, G., Krause, O., Groves, B., Sandstrom, K., Braun, R., Leroy, A., Klaas, U., Linz, H., Rix, H.-W., Schinnerer, E., Schmiedeke, A., & Walter, F. 2014, *ApJ*, 780, 172
- Draine, B. T., Dale, D. A., Bendo, G., Gordon, K. D., Smith, J. D. T., Armus, L., Engelbracht, C. W., Helou, G., Kennicutt, Jr., R. C., Li, A., Roussel, H., Walter, F., Calzetti, D., Moustakas, J., Murphy, E. J., Rieke, G. H., Bot, C., Hollenbach, D. J., Sheth, K., & Teplitz, H. I. 2007, *ApJ*, 663, 866
- Fan, X., Strauss, M. A., Becker, R. H., White, R. L., Gunn, J. E., Knapp, G. R., Richards, G. T., Schneider, D. P., Brinkmann, J., & Fukugita, M. 2006, *AJ*, 132, 117
- Fisher, D. B., Bolatto, A. D., Herrera-Camus, R., Draine, B. T., Donaldson, J., Walter, F., Sandstrom, K. M., Leroy, A. K., Cannon, J., & Gordon, K. 2014, *Nature*, 505, 186
- Fruchter, A. S., Levan, A. J., Strolger, L., Vreeswijk, P. M., Thorsett, S. E., Bersier, D., Burud, I., Castro Cerón, J. M., Castro-Tirado, A. J., Conselice, C., Dahlen, T., Ferguson, H. C., Fynbo, J. P. U., Garnavich, P. M., Gibbons, R. A., Gorosabel, J., Gull, T. R., Hjorth, J., Holland, S. T., Kouveliotou, C., Levay, Z., Livio, M., Metzger, M. R., Nugent, P. E., Petro, L., Pian, E., Rhoads, J. E., Riess, A. G., Sahu, K. C., Smette, A., Tanvir, N. R., Wijers, R. A. M. J., & Woosley, S. E. 2006, *Nature*, 441, 463
- Greiner, J., Krühler, T., Fynbo, J. P. U., Rossi, A., Schwarz, R., Klose, S., Savaglio, S., Tanvir, N. R., McBreen, S., Totani, T., Zhang, B. B., Wu, X. F., Watson, D., Barthelmy, S. D., Beardmore, A. P., Ferrero, P., Gehrels, N., Kann, D. A., Kawai, N., Yoldaş, A. K., Mészáros, P., Milvang-Jensen, B., Oates, S. R., Pierini, D., Schady, P., Toma, K., Vreeswijk, P. M., Yoldaş, A., Zhang, B., Afonso, P., Aoki, K., Burrows, D. N., Clemens, C., Filgas, R., Haiman, Z., Hartmann, D. H., Hasinger, G., Hjorth, J., Jehin, E., Levan, A. J., Liang, E. W., Malesani, D., Pyo, T.-S., Schulze, S., Szokoly, G., Terada, K., & Wiersema, K. 2009, *ApJ*, 693, 1610
- Hahn, O., & Abel, T. 2011, *MNRAS*, 415, 2101
- Kawai, N., Kosugi, G., Aoki, K., Yamada, T., Totani, T., Ohta, K., Iye, M., Hattori, T., Aoki, W., Furusawa, H., Hurley, K., Kawabata, K. S., Kobayashi, N., Komiyama, Y., Mizumoto, Y., Nomoto, K., Noumaru, J., Ogasawara, R., Sato, R., Sekiguchi, K., Shirasaki, Y., Suzuki, M., Takata, T., Tamagawa, T., Terada, H., Watanabe, J., Yatsu, Y., & Yoshida, A. 2006, *Nature*, 440, 184
- Kimm, T., & Cen, R. 2013, *ApJ*, 776, 35
- . 2014, *ApJ*, 788, 121
- Knollmann, S. R., & Knebe, A. 2009, *ApJS*, 182, 608
- Komatsu, E., Smith, K. M., Dunkley, J., Bennett, C. L., Gold, B., Hinshaw, G., Jarosik, N., Larson, D., Nolta, M. R., Page, L., Spergel, D. N., Halpern, M., Hill, R. S., Kogut, A., Limon, M., Meyer, S. S., Odegard, N., Tucker, G. S., Weiland, J. L., Wollack, E., & Wright, E. L. 2011, *ApJS*, 192, 18

- Konami, S., Matsushita, K., Tsuru, T. G., Gandhi, P., & Tamagawa, T. 2011, PASJ, 63, 913
- Krumholz, M. R., & Tan, J. C. 2007, ApJ, 654, 304
- Lamb, D. Q., & Reichart, D. E. 2000, ApJ, 536, 1
- Larson, R. B. 1969, MNRAS, 145, 271
- Laskar, T., Berger, E., Tanvir, N., Zauderer, B. A., Margutti, R., Levan, A., Perley, D., Fong, W.-f., Wiersema, K., Menten, K., & Hrudkova, M. 2014, ApJ, 781, 1
- Le Floch, E., Charmandaris, V., Gordon, K., Forrest, W. J., Brandl, B., Schaerer, D., Dessauges-Zavadsky, M., & Armus, L. 2012, ApJ, 746, 7
- Martin, C. L., Kobulnicky, H. A., & Heckman, T. M. 2002, ApJ, 574, 663
- Nardini, M., Ghisellini, G., & Ghirlanda, G. 2008, MNRAS, 386, L87
- Penston, M. V. 1969, MNRAS, 144, 425
- Rosdahl, J., Blaizot, J., Aubert, D., Stranex, T., & Teyssier, R. 2013, ArXiv e-prints
- Sari, R., Piran, T., & Narayan, R. 1998, ApJ, 497, L17
- Schady, P., Savaglio, S., Krühler, T., Greiner, J., & Rau, A. 2011, A&A, 525, A113
- Schmidt, M. 1959, ApJ, 129, 243
- Tanvir, N. R., Fox, D. B., Levan, A. J., Berger, E., Wiersema, K., Fynbo, J. P. U., Cucchiara, A., Krühler, T., Gehrels, N., Bloom, J. S., Greiner, J., Evans, P. A., Rol, E., Olivares, F., Hjorth, J., Jakobsson, P., Farihi, J., Willingale, R., Starling, R. L. C., Cenko, S. B., Perley, D., Maund, J. R., Duke, J., Wijers, R. A. M. J., Adamson, A. J., Allan, A., Bremer, M. N., Burrows, D. N., Castro-Tirado, A. J., Cavanagh, B., de Ugarte Postigo, A., Dopita, M. A., Fatkhullin, T. A., Fruchter, A. S., Foley, R. J., Gorosabel, J., Kennea, J., Kerr, T., Klose, S., Krimm, H. A., Komarova, V. N., Kulkarni, S. R., Moskvitin, A. S., Mundell, C. G., Naylor, T., Page, K., Penprase, B. E., Perri, M., Podsiadlowski, P., Roth, K., Rutledge, R. E., Sakamoto, T., Schady, P., Schmidt, B. P., Soderberg, A. M., Sollerman, J., Stephens, A. W., Stratta, G., Ukwatta, T. N., Watson, D., Westra, E., Wold, T., & Wolf, C. 2009, Nature, 461, 1254
- Teyssier, R. 2002, A&A, 385, 337
- Totani, T., Aoki, K., Hattori, T., Kosugi, G., Niino, Y., Hashimoto, T., Kawai, N., Ohta, K., Sakamoto, T., & Yamada, T. 2013, ArXiv e-prints
- Totani, T., Kawai, N., Kosugi, G., Aoki, K., Yamada, T., Iye, M., Ohta, K., & Hattori, T. 2006, PASJ, 58, 485

- Zafar, T., Watson, D., Elíasdóttir, Á., Fynbo, J. P. U., Krühler, T., Schady, P., Leloudas, G., Jakobsson, P., Thöne, C. C., Perley, D. A., Morgan, A. N., Bloom, J., & Greiner, J. 2012, *ApJ*, 753, 82
- Zafar, T., Watson, D. J., Malesani, D., Vreeswijk, P. M., Fynbo, J. P. U., Hjorth, J., Levan, A. J., & Michałowski, M. J. 2010, *A&A*, 515, A94